Article

Simple Preparation of LaPO$_4$:Ce, Tb Phosphors by an Ionic-Liquid-Driven Supported Liquid Membrane System

Jianguo Li [1,3]**, Hongying Dong** [1,]*****, Fan Yang** [2,3,]***** [ID]**, Liangcheng Sun** [3,4]**, Zhigang Zhao** [2,3]**, Ruixi Bai** [2,3] **and Hao Zhang** [2,3]

[1]   School of Chemical Engineering, Inner Mongolia University of Technology, Hohhot 010051, China
[2]   Key Laboratory of Design and Assembly of Functional Nanostructures, Fujian Provincial Key Laboratory of Nanomaterials, Fujian Institute of Research on the Structure of Matter, Chinese Academy of Sciences, Xiamen 361021, China
[3]   Xiamen Institute of Rare Earth Materials, Chinese Academy of Sciences, Xiamen 361021, China
[4]   Baotou Research Institute of Rare Earths, Baotou 014030, China
*   Correspondence: donghongying@imut.edu.cn (H.D.); fanyang2013@fjirsm.ac.cn (F.Y.);
     Tel.: +86-0471-6575722 (H.D.); +86-157-5073-3599 (F.Y.)

check for
updates

Abstract: In this work, LaPO$_4$:Ce, Tb phosphors were prepared by firing a LaPO$_4$:Ce, Tb precipitate using an ionic-liquid-driven supported liquid membrane system. The entire system consisted of three parts: a mixed rare earth ion supply phase, a phosphate supply phase, and an ionic-liquid-driven supporting liquid membrane phase. This method showed the advantages of a high flux, high efficiency, and more controllable reaction process. The release rate of PO$_4^{3-}$ from the liquid film under different types of ionic liquid, the ratio of the rare earth ions in the precursor mixture, and the structure, morphology, and photoluminescence properties of LaPO$_4$:Ce, Tb were investigated by inductively coupled plasma-atomic emission spectroscopy, X-ray diffraction, Raman spectra, scanning electron microscopy, and photoluminescence emission spectra methods. The results showed that a pure phase of lanthanum orthophosphate with a monoclinic structure can be formed. Due to differences in the anions in the rare earth supply phase, the prepared phosphors showed micro-spherical (when using rare earth sulfate as the raw material) and nanoscale stone-shape (when using rare earth nitrate as the raw material) morphologies. Moreover, the phosphors prepared by this method had good luminescent properties, reaching a maximum emission intensity under 277 nm excitation with a predominant green emission at 543 nm which corresponded to the $^5D_4$-$^7F_5$ transition of Tb^{3+}.

Keywords: LaPO$_4$: Ce; Tb; ionic liquid; supported liquid membrane; photoluminescence

1. Introduction

Recently, rare-earth-ion-doped multicomponent compounds have attracted considerable attention due to their potential applications in the fields of electroluminescent devices, high-resolution displays, biological labels, and integrated optics [1–4]. Among these rare-earth-doped oxide phosphors, trivalent-cerium- and terbium-coactivated LaPO$_4$ is significant because of its low solubility in water, its high thermal stability, and its high-efficiency energy transfer between Ce^{3+} and Tb^{3+} [5–8]. Due to the 4f orbital properties of La^{3+}, lanthanide phosphate is transparent in the visible region and has been proven to be an ideal host structure for other lanthanide ions, resulting in luminescent materials in the UV-visible region [9–11]. In Ce^{3+} and Tb^{3+} co-doped LaPO$_4$, Ce^{3+} with optically allowed d–f transitions is an effective activator for Tb^{3+} emission [12,13]. LaPO$_4$:Ce^{3+}, Tb^{3+} powders have been widely used as the green component of three band emission type fluorescent lamps [14,15]. In addition,

$LaPO_4:Ce^{3+}$, Tb^{3+} phosphors have drawn continuous research attention in several other applications, including transparent fillers/markers, biomedical purposes, and plasma display panels [13,16–18].

Phosphor particles should be spherical in shape with no aggregation and their particle size should be in the micron range (<3 μm) with a narrow size distribution [16,19]. Spherical phosphor particles are more advantageous for the optical and geometric structure of the phosphor layer. The size of the phosphor affects the number of phosphor particles needed to produce the best coating for a particular application [20]. The shape, size distribution, and other microstructural characteristics of phosphors can be well controlled by different synthetic methods and reaction conditions. To date, several methods have been reported for the synthesis of phosphate phosphor materials, such as coprecipitation [21–23], solvothermal methods [24,25], electrospinning methods [26], solid-state methods [27], sol-gel processes [10,12], and spray pyrolysis [14]. Of these, coprecipitation is a common industrial synthetic method used to produce rare earth oxide powders and has the advantages of being feasible, low-cost, and environmentally friendly. Beyond that, fluorescent powders prepared by the coprecipitation method have uniform particle sizes, low agglomeration, and low phase impurities [21]. However, many factors such as reaction temperature, aging time, pH value, and solution concentration need to be controlled, which limits the development of coprecipitation methods. It is still challenging to simply prepare phosphors with favorable morphologies and excellent luminescent performance.

Ionic liquids are a kind of green solvent which includes a wide range of liquids, excellent thermal stability, a wide electrochemical window, and a low vapor pressure [28–32]. Recently, much attention has been paid to the study of ionic liquids in supported liquid membrane systems [33,34]. Ionic-liquid-driven supported liquid membrane systems have shown the advantages of high flux, high efficiency, strong durability, and environmental friendliness, and have made great progress in gas separation, organic separation, metal ion separation, and chemical reactions. Our team first committed to the use of an ionic-liquid-driven supported liquid membrane system to prepare $CePO_4$ inorganic nanomaterials. In doing so, we could easily control the morphologies (rod or sphere) of rare earth luminescent materials by adjusting the pH and the concentration of SO_4^{2-} [34]. Here, we used a facile ionic-liquid-driven supported liquid membrane method to prepare rare earth ion (Ce^{3+}, Tb^{3+}) co-doped $LaPO_4$ phosphors with different morphologies (spherical and stone-like shapes). The preparation procedure, the role of the ionic liquid supported liquid membrane, characterization of the crystal structure, and photoluminescent properties of the synthesized $LaPO_4:Ce^{3+}$, Tb^{3+} phosphors are reported in the following sections. This method has been proven to be easily controlled, simple, and mild, and the phosphors prepared by this method show good morphological and photoluminescent properties.

2. Results and Discussion

2.1. Ionic-Liquid-Driven HVHP Membrane Characterization

In this experiment, we use a microporous ionic-liquid-driven HVHP membrane as selective ion channels that can selectively transfer PO_4^{3-} from the PO_4^{3-} supply phase into the mixed rare earth ion supply phase to prepare phosphors. We referred to the methods of Krzysztof A. et al. [35] to characterize the ionic-liquid-driven HVHP membrane. A Raman study was performed to investigate the ionic liquid presence on the surface and inside the HVHP membrane. The spectra of the inner part of the ionic-liquid-driven HVHP membrane was recorded up to 40 μm below the surface. As shown in Figure 1, the Raman vibration modes of ionic liquids can be observed on the surface of and in the interior of their corresponding functional membranes, which proves ionic liquids' presence on the surface and inside the HVHP membranes. Figure 2 shows SEM micrographs of the cross-section of the untreated HVHP membrane, as well as SEM micrographs and the corresponding map microanalysis (B or S) of the cross-section of the resulting [C_4mim][BF_4]- and [C_4mim][Tf_2N]-driven HVHP membranes. The micrographs and map microanalysis show that the ionic liquid infiltrates the reticular surface of the membrane.
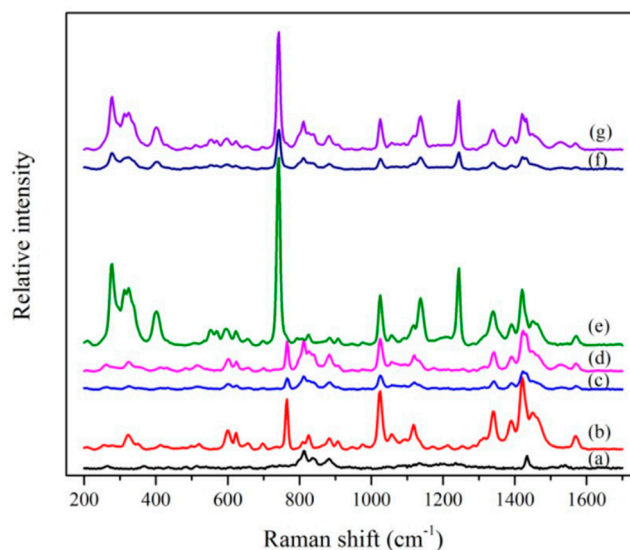
Figure 1. Comparison of Raman spectra of (a) untreated HVHP membrane, (b) [C_4mim][BF_4], (c) the surface of the [C_4mim][BF_4]-driven HVHP, (d) the internal part (40 μm below the surface) of the [C_4mim][BF_4]-driven HVHP, (e) [C_4mim][Tf_2N], (f) the surface of the [C_4mim][Tf_2N]-driven HVHP membrane and (g) the internal part (40 μm below the surface) of the [C_4mim][Tf_2N]-driven HVHP membrane.
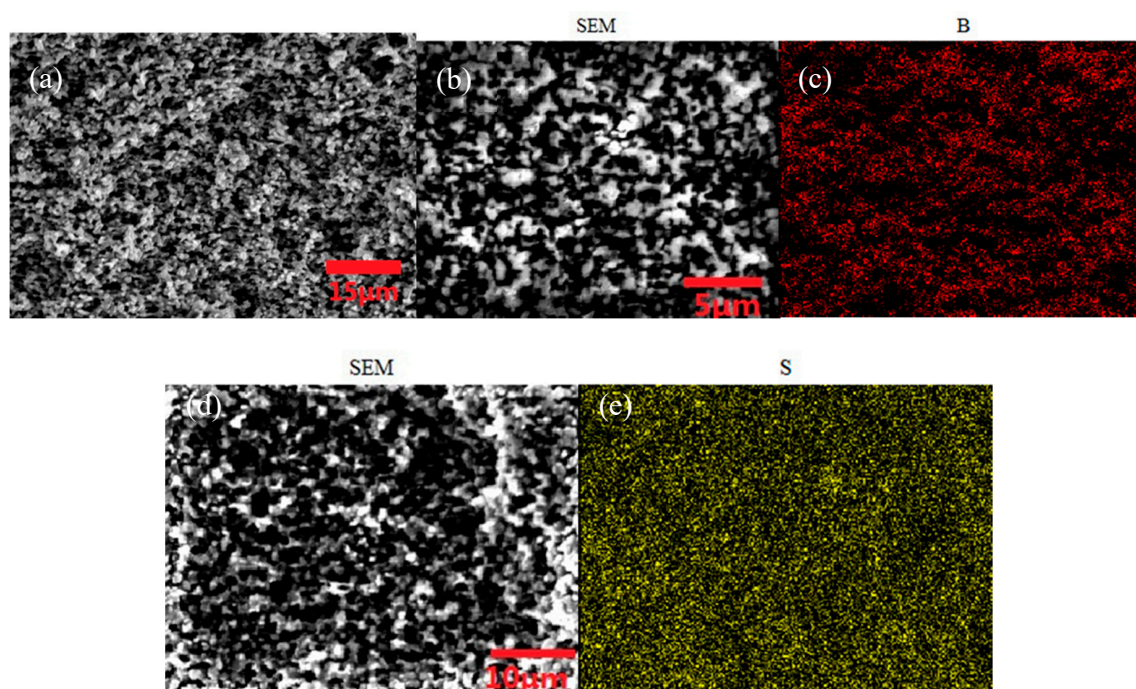

Figure 2. Plot of (**a**) micrographs of the cross-section of the untreated HVHP membrane, (**b**) micrographs of the cross-section of the [C_4mim][BF_4]-driven HVHP, (**c**) map microanalysis (B) of [C_4mim][BF_4]-driven HVHP, (**d**) micrographs of the cross-section of [C_4mim][Tf_2N] and (**e**) map microanalysis (S) of the [C_4mim][Tf_2N]-driven HVHP membrane.

2.2. Membrane Reaction Mechanism

We referred to the mechanism study of PanPan Zhao et al. [34] to propose a possible membrane reaction mechanism. The entire process can be divided into two parts: the liquid membrane transport stage and the precipitation reaction stage. The porous HVHP membrane is a good hydrophobic barrier which can effectively separate the two aqueous phases. After being immersed in an ionic

liquid, the function of the HVHP film changes significantly. The microporous HVHP membrane containing an ionic liquid consists of selective ion channels which can selectively transfer PO_4^{3-} from the PO_4^{3-} supply phase into the mixed rare earth ion supply phase; the microporous HVHP membrane without ionic liquid cannot do this (Figure 3a). A precipitation reaction occurs upon PO_4^{3-} contacting the mixed rare earth ion supply phase on the other side of the HVHP membrane. Throughout the process, the cation (imidazolium) of the ionic liquid is responsible for the selective transfer of PO_4^{3-} from the PO_4^{3-} supply phase to the mixed rare earth ion supply phase. The anion is responsible for controlling the mixed rare earth ion supply phase and the release rate and ionic liquid hydrophobicity are correlated [34]. The hydrophilicity follows the order $[N(SO_2CF_3)_2]^- < [BF_4]^-$, so the release rate of PO_4^{3-} of the ionic-liquid-driven HVHP membrane is in this order (Figure 3a). The reaction appears to be a liquid-liquid extraction and occurs in the ionic liquid-film phase at the membrane interface. In addition, due to the thinness and high porosity of the porous HVHP membrane, the numerous ion transport channels are very short, meaning the precipitation reaction occurs quickly and efficiently. The experimental device and a schematic diagram of the reaction mechanisms are shown in Figure 4.
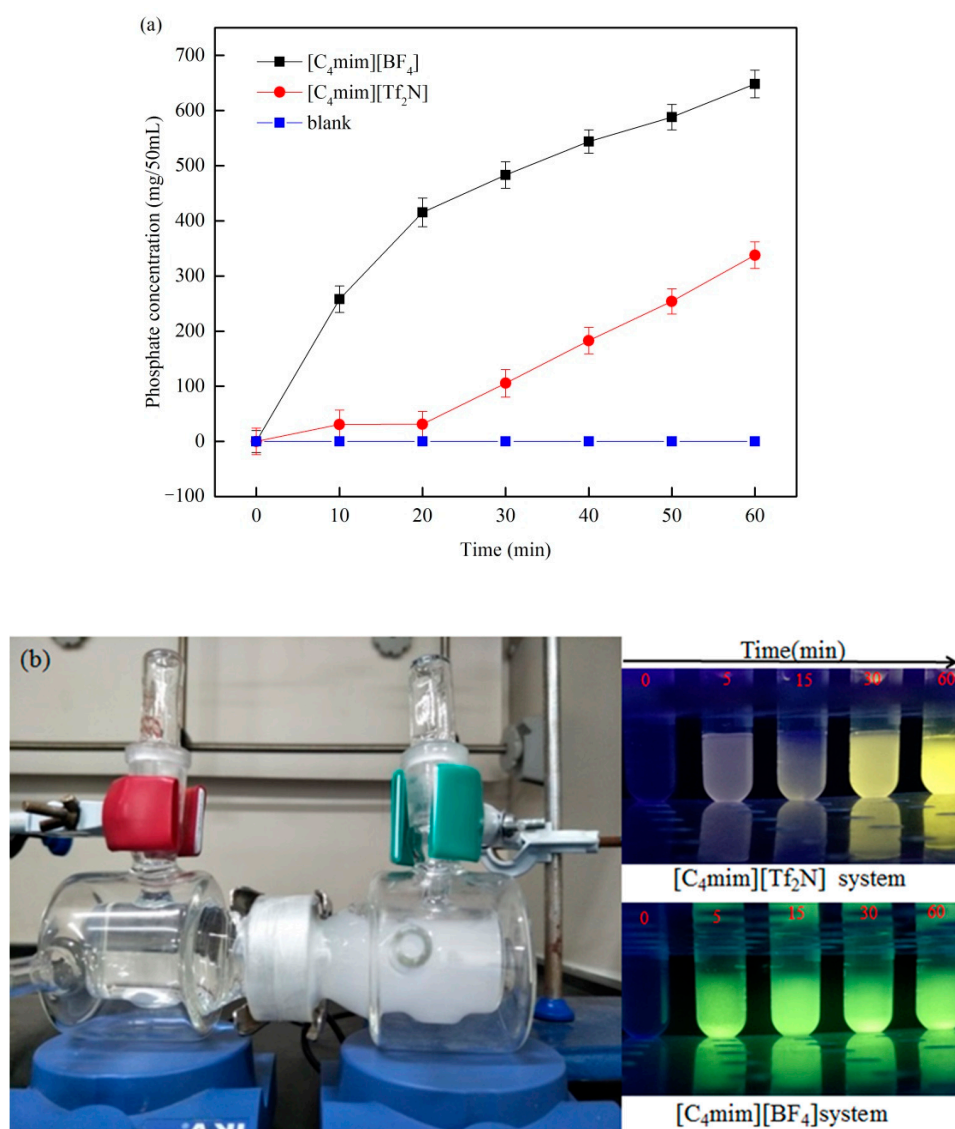

Figure 3. Plot of (**a**) the concentration of PO_4^{3-} that has crossed the liquid membrane within 60 min using different ionic liquids in the liquid membrane phase and (**b**) picture of the phosphor reaction process and images of the precursor solution color within 60 min when using different ionic liquids in the liquid membrane phase.
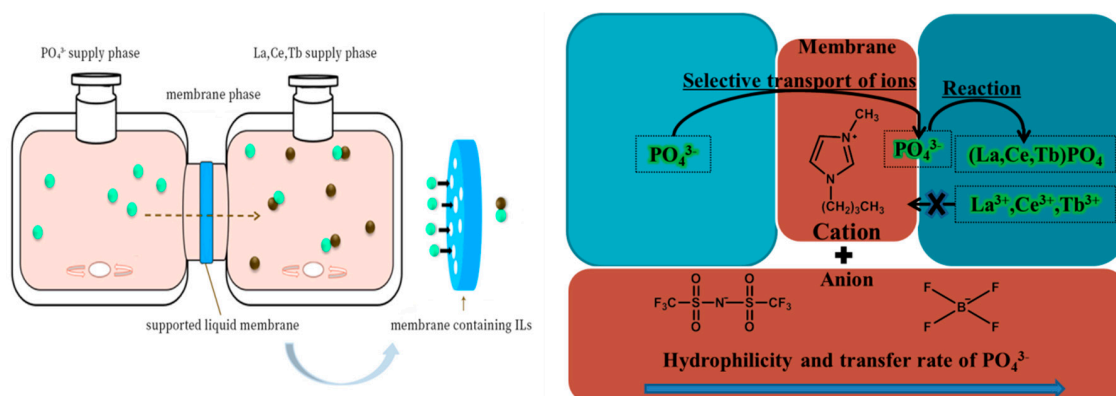
Figure 4. Ionic-liquid-driven supported liquid membrane system and schematic diagram of reaction mechanism.

2.3. Transmittance of PO_4^{3-} under the Action of the Two Functional Membranes

To investigate the transfer efficiency of PO_4^{3-} by the different functional membranes, we performed the following experiment devices: two glass units sandwiching blank-, [C$_4$mim][BF$_4$]- or [C$_4$mim][Tf$_2$N]-infiltrated membranes. The glass units were filled with 50 mL deionized water and 50 mL of the phosphoric acid solution (1 M). To ensure a homogeneous system, both solutions were stirred with a magnetic stirrer at 1000 rpm. Samples of 10 μL were taken from the deionized water phase every 10 min. Then, the samples were diluted and the transfer of PO_4^{3-} under the action of three kinds of membranes was measured with ICP. Figure 3a shows the changes of PO_4^{3-} concentration in 50 mL of a deionized water phase under the action of three different membranes within 60 min. The PO_4^{3-} concentration remained at 0 under the action of the blank-infiltrated membrane while the PO_4^{3-} concentration increased under the action of the ionic liquid functional membranes. This suggests that PO_4^{3-} cannot cross the blank-infiltrated membrane but can cross ionic liquid functional membranes. There is a clear difference between the [C$_4$mim][BF$_4$] functional membrane and the [C$_4$mim][Tf$_2$N] functional membrane, which indicates that the transfer efficiency of the [C$_4$mim][BF$_4$] functional membrane toward PO_4^{3-} is much greater than that of the [C$_4$mim][Tf$_2$N] functional membrane. Figure 3b shows a picture of the phosphor reaction process and images of the precursor solution color when using rare earth sulfates as the rare earth supply phase for the different ionic liquid systems at different times under 254 nm irradiation. As shown in Figure 3b, precipitation occurs only in the rare earth phases, which indicates that the rare earth ions cannot pass through the membrane channels but phosphate can. The sample solutions all emitted green fluorescence when under a 254 nm light source and the fluorescence brightness increased with increasing reaction time. This proves that the membrane transfer rate of PO_4^{3-} for the [C$_4$mim][BF$_4$] functional membrane is markedly faster than that for the [C$_4$mim][Tf$_2$N] functional membrane, which is consistent with the results of previous research. In the actual production application, we can choose an appropriate functional membrane with different ionic liquids to achieve the effect of controlling the rate of production.

2.4. Study of the Proportion of $LaPO_4:Ce^{3+}, Tb^{3+}$

To explore the proportion of product, we dissolved an appropriate amount of the precursor (preparation conditions: 1 mol phosphoric acid solution, rare earth sulfate solution, and [C$_4$mim][Tf$_2$N] functional membrane) in a moderate amount of hydrochloric acid at 60 °C for 30 min, diluted the sample to the right concentration, and then tested the rare earth ion concentration by ICP. Table 1 shows the molar ratio of the mixed solution of rare earth elements from the rare earth supply phase and the molar ratio of the precursor. A clear difference between the solution proportion and precursor proportion can be seen in Table 1 because the rare earth ions do not completely precipitate. Then,

we obtained the molar ratio (a fitting degree of greater than 99%) commonly used in the production of phosphate (La:Ce:Tb = 55:30:15) by simply adjusting the molar ratio of the rare earth ions in solution.

Table 1. The molar ratio of a mixed solution of the rare earth elements and the molar ratio of the precursor.

Samples	La^{3+} Molal Percent	Ce^{3+} Molal Percent	Tb^{3+} Molal Percent
Initial solution	55.13	31.04	13.83
Initial precursors	53.40	34.99	11.61
After adjusting solution	55.70	26.20	18.09
After adjusting precursors	55.00	30.11	14.89

2.5. Structure and Morphologies of the LaPO$_4$:Ce^{3+}, Tb^{3+} Phosphors

In this study, we used an ionic-liquid-driven supported liquid membrane system to prepare phosphors. The whole system consisted of two glass units sandwiching a functional membrane ([C$_4$mim][BF$_4$] or [C$_4$mim][Tf$_2$N]). The glass units were filled with 50 mL of the rare earth mixture (rare earth sulfates or rare earth nitrates) and 50 mL of the phosphoric acid solution (1 M). The PO$_4$$^{3-}$ crossed the functional membrane to react with the rare earth ions in this system. Finally, the phosphors were prepared by calcining the precursors. The powder samples prepared from different rare earth ion sources (rare earth nitrates and rare earth sulfates) in the [C$_4$mim][BF$_4$] functional membrane were labelled BN and BS, respectively, and powder samples prepared from different rare earth ion sources (rare earth nitrates and rare earth sulfates) in the [C$_4$mim][Tf$_2$N] functional membrane were labelled NN and NS, respectively.

X-ray diffraction patterns were employed to determine the phase purities and crystal structures of the phosphor products. Figure 5a shows the XRD patterns of the precursors prepared under different conditions (different rare earth solutions and different ionic liquids). The vertical bars show the standard hexagonal LaPO$_4$ peak positions (JCPDS No. 04-0635). Figure 5a shows that the diffraction peaks of all the precursors can be readily indexed to the hexagonal structure of LaPO$_4$ in the P6222 space group (JCPDS No 04-0635). Figure 5b shows the XRD patterns of the as-prepared LaPO$_4$:Ce, Tb phosphor samples prepared under different conditions (different rare earth solutions and different ionic liquids). The vertical bars show the standard monoclinic LaPO$_4$ peak positions (JCPDS No. 32-0493). From Figure 5b, it is obvious that peaks at 2θ = 19.04°, 21.74°, 27.08°, 28.88°, and 42.48° are present after annealing at 1000 °C, which may be attributed to the (011), (101), (200), (120), and (221) reflections of the monazite crystalline structure of lanthanum phosphate. A monoclinic phase (space group: P21/n) of pure LaPO$_4$ (JCPDS No. 32-0943) was obtained. By comparing the XRD pattern of the as-prepared precursors and LaPO$_4$:Ce, Tb phosphor samples, we found that after annealing at 1000 °C, the fluorescent powder XRD peaks were sharper, the crystallinity was better and the structure of LaPO$_4$:Ce, Tb had changed from a hexagonal to a monoclinic crystal phase. In addition, after the sample was calcined at 1000 °C, all the diffraction peaks shifted to the right compared with the standard diffraction peaks. This is because the radii of Ce^{3+} (~0.1034 nm) and Tb^{3+} (~0.0923 nm) are smaller than the radius of La^{3+} (~0.1061 nm) in the LaPO$_4$:Ce^{3+}, Tb^{3+} crystals, which leads to lattice contraction and a reduction of interplanar distance. Thus, based on the Bragg diffraction principle 2dsinθ = λ, where the decrease of the d value increases the diffraction angle, the diffraction peak positions of the XRD patterns move towards larger angles [23,36].

The morphology, size, and microstructural details were investigated by scanning electron microscopy. Figure 6 shows the SEM micrographs of the precursors prepared under different conditions (different rare earth solutions and different ionic liquids). Notably, the morphologies of the precursors are similar in the different ionic liquid functional membranes but show different morphologies for the different rare earth sources. When the anion of the rare earth mixed solution was sulfate, the samples exhibited a spherical morphology with particle sizes in the range of 600–800 nm, and a rough surface which consisted of aggregates of smaller particles. When the anion of the rare

earth mixed solution was nitrate, the samples exhibited a flower-like structure with a diameter of approximately 30 nm and a length of approximately 200 nm. According to our previous research, we believe the reason for the formation of this globular structure is due to the template effect of SO_4^{2-} [34]. Figure 7 shows SEM micrographs of the as-prepared $LaPO_4$:Ce, Tb phosphor samples prepared under different conditions (different rare earth solutions and different ionic liquids). Similarly to the precursors, the annealed samples had similar morphologies when prepared with different ionic liquid functional membranes but different morphologies when prepared with different rare earth sources. After sintering, the samples prepared with rare earth sulfates as the raw material maintained their spherical structure, but the aggregation between spheres was more severe than that in the precursor samples. The small particles on the spherical surface of the sintered samples were larger than those on the surface of the respective precursor. However, after sintering, the samples prepared with rare earth nitrates as the raw material changed from a nanowire flower-like structure to a stone-like structure. The particle sizes were in the range 30–300 nm. The results show that the crystal size of all the samples increased after calcining, and due to the templating effect of SO_4^{2-}, the samples with rare earth sulfates as the raw material continued to maintain their large micro-sized spherical morphology, while the shape of the samples prepared using rare earth nitrates as the raw material grew from a flower-like structure into a stone-like morphology.
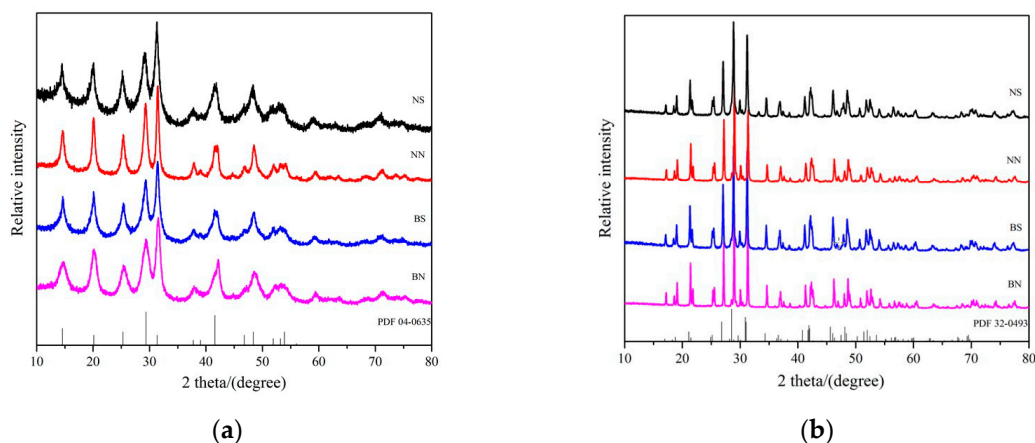

(**a**)   (**b**)

Figure 5. XRD patterns of the precursors (**a**) and calcined $LaPO_4$:Ce^{3+}, Tb^{3+} phosphors (**b**) prepared under different conditions.
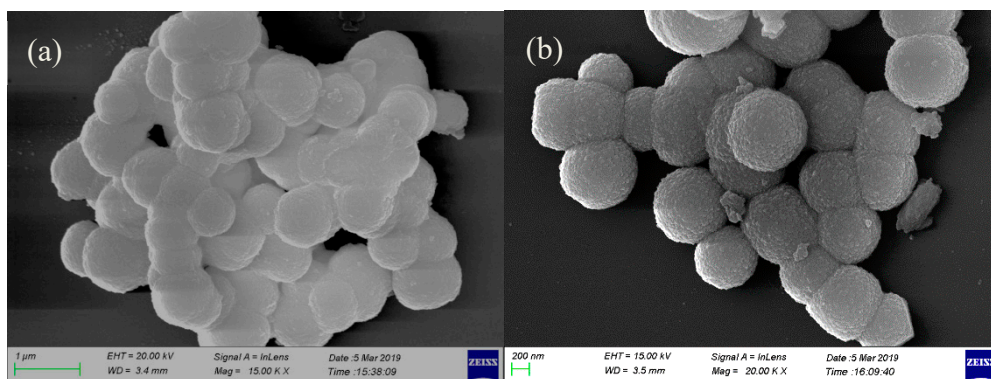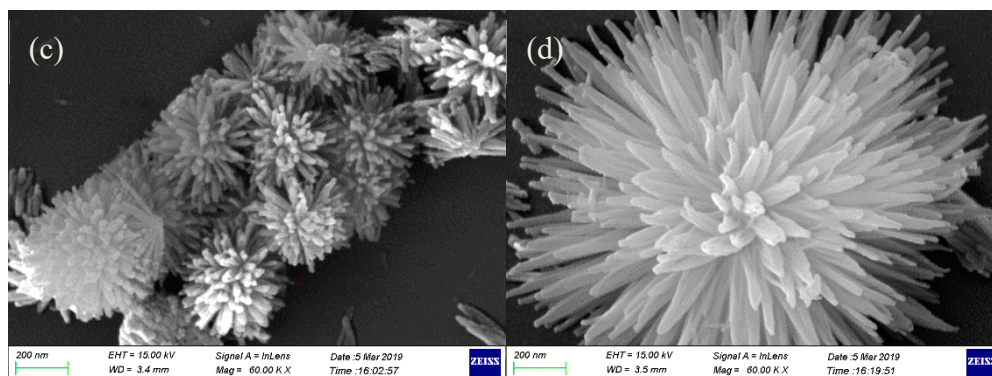

Figure 6. *Cont.*

Figure 6. SEM images of the precursors prepared under different conditions: (**a**) BS, (**b**) NS, (**c**) BN, and (**d**) NN. (EHT for extra high tension, WD for working distance)
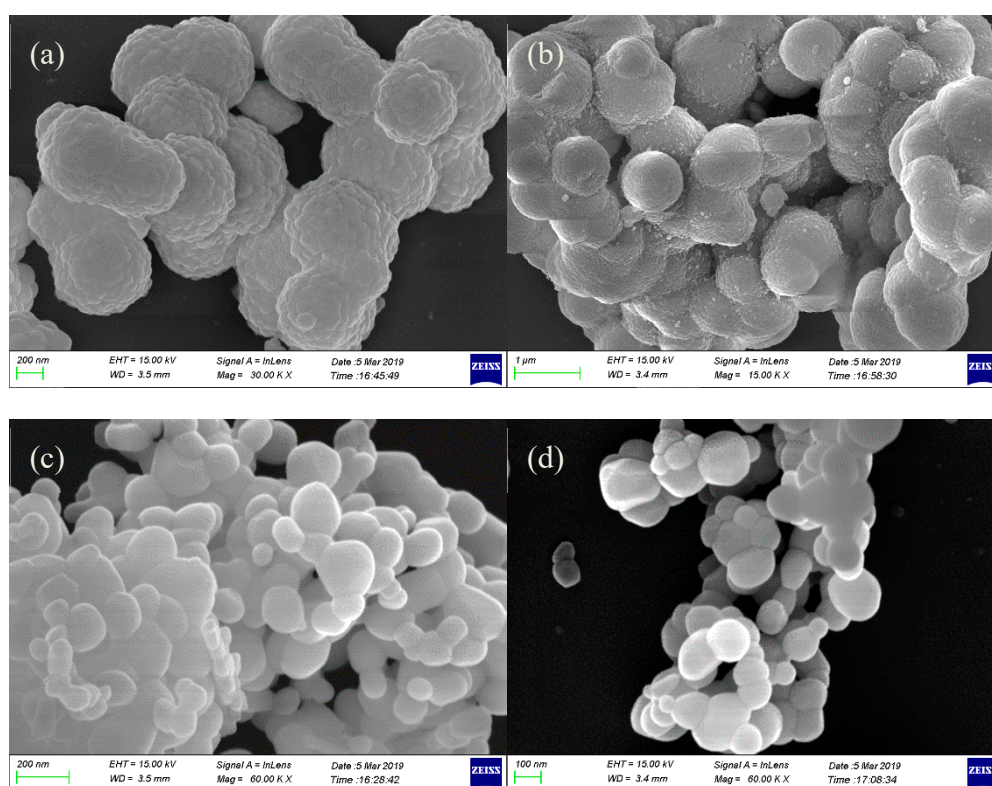

Figure 7. SEM images of calcined $LaPO_4$:Ce^{3+}, Tb^{3+} phosphors prepared under different conditions: (**a**) BS, (**b**) NS, (**c**) BN, and (**d**) NN. (EHT for extra high tension, WD for working distance)

2.6. Photoluminescent Properties of the $LaPO_4$:Ce^{3+}, Tb^{3+} Phosphors

Figure 8 shows the excitation spectra of all the calcined $LaPO_4$:Ce^{3+}, Tb^{3+} phosphors by monitoring the $^5D_4 \rightarrow {}^7F_5$ emission of Tb^{3+} (λ_{em} = 543 nm) at room temperature. As clearly shown in Figure 8, the obtained fluorescent materials absorb excitation energy in the range of 240–310 nm with a maximum excitation wavelength at 277 nm, which may be related to the f–d transitions of Ce^{3+}. In addition, several small peaks can be detected in the range of 310–400 nm, which could be caused by the f–f transitions of Tb^{3+} [37,38]. Because of the forbidden nature of these transitions, their oscillator strength is much weaker than that of the spin-allowed $4f^1$–$4f^0 5d^1$ Ce^{3+} transitions [22]. The excitation spectra consist of the strong excitation band of Ce^{3+} and the weak excitation bands of Tb^{3+}, revealing that Tb^{3+} are essentially excited by Ce^{3+}. In fact, several of the weak f–f excitation bands of Tb^{3+} are only present in the region of the Ce^{3+} emission. Thus, energy transfer from Ce^{3+} to Tb^{3+} occurs [21]. The emission spectra of all the calcined $LaPO_4$:Ce^{3+}, Tb^{3+} phosphors at an excitation of 277 nm are shown in Figure 9.

All the calcined $LaPO_4$:Ce^{3+}, Tb^{3+} phosphors show obvious photoluminescence in the spectral range of 450–650 nm, and the four emission peaks at 487, 543, 584, and 621 nm can be assigned to the $^5D_4$–$^7F_6$, $^5D_4$–$^7F_5$, $^5D_4$–$^7F_4$, and $^5D_4$–$^7F_3$ transitions, respectively, of Tb^{3+} [39,40]. Among these peaks, the green emission at 543 nm, which corresponds to the $^5D_4$–$^7F_5$ transition of Tb^{3+}, is the predominant peak. The spectral properties of the phosphors prepared by an ionic-liquid-driven supported liquid membrane system are essentially the same as those prepared by other synthetic methods, in which the improved ionic-liquid-driven supported liquid membrane system is a new and effective method to prepare $LaPO_4$:Ce^{3+}, Tb^{3+} phosphors.
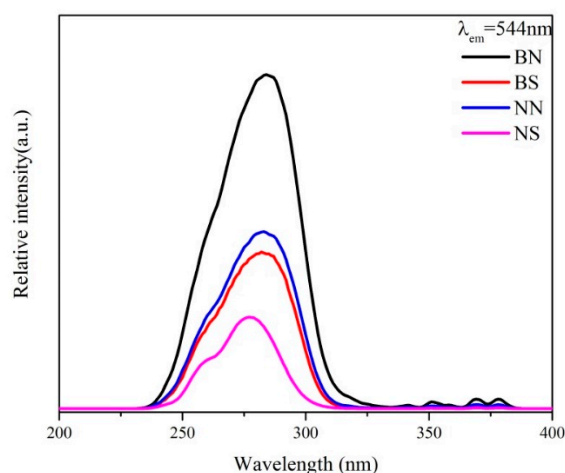
Figure 8. The excitation spectra of the calcined $LaPO_4$:Ce^{3+}, Tb^{3+} phosphors prepared under different conditions.
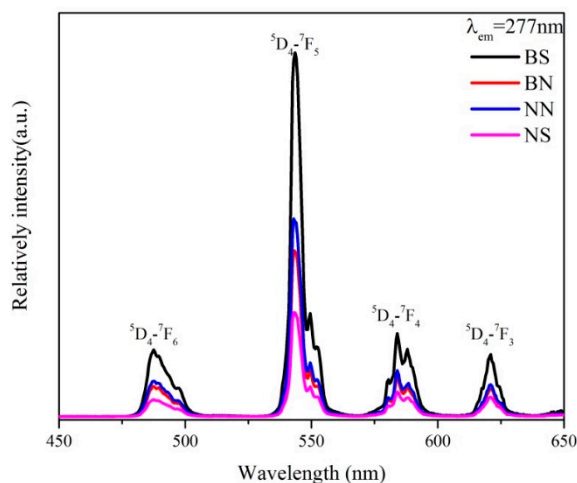

Figure 9. The emission spectra of the calcined $LaPO_4$: Ce^{3+}, Tb^{3+} phosphors prepared under different conditions.

3. Materials and Methods

3.1. Materials

The lanthanum sulfate hydrate, cerium sulfate hydrate, terbium sulfate hydrate, lanthanum nitrate hydrate, cerium nitrate hydrate, and terbium nitrate hydrate were provided by the Baotou Research Institute of Rare Earths, and the phosphoric acid solution was purchased from Aladdin (Shanghai, China). The chemicals used in the experiments were of analytical grade. The HVHP-04700 (pore size 0.45 μm and thickness 125 μm, ø: 5.5 cm, DUPAPORE®), a hydrophobic porous polyvinylidene fluoride film, was obtained from Millipore Corp. The ionic liquids (ILs) were selected from [C_4mim][BF_4]

and [C$_4$mim][Tf$_2$N] produced by the Center for Green Chemistry and Catalysis, Lanzhou Institute of Chemical Physics, Chinese Academy of Sciences. Figure 10 shows the molecular structures of the ionic liquids used in this study.
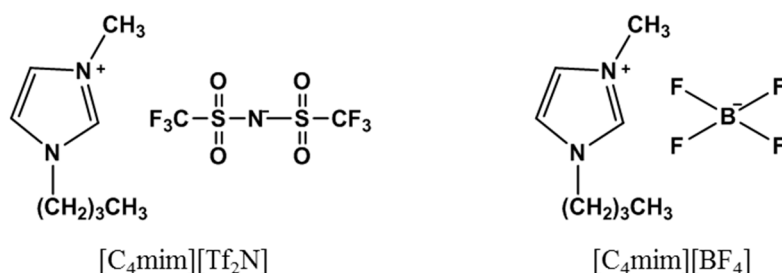

Figure 10. The molecular structures of the different ionic liquids used.

3.2. Preparation of the Ionic-Liquid-Driven Supported Liquid Membrane, the La, Ce, and Tb Supply Phase, and the PO$_4{}^{3-}$ Supply Phase

To prepare the ionic-liquid-driven supported liquid membrane, the hydrophobic porous polyvinylidene fluoride film (HVHP-04700) was immersed in an ionic liquid ($\geq$200 μL of either [C$_4$mim][BF$_4$] or [C$_4$mim][Tf$_2$N]) for more than 2 h. For the La, Ce, and Tb supply phase, a lanthanum sulfate, cerium sulfate, and terbium sulfate mixed solution (or a lanthanum nitrate, cerium nitrate, and terbium nitrate mixed solution) was prepared in a calibrated volumetric flask by dissolving each compound in ultrapure water at a suitable La/Ce/Tb molar ratio. Each compound was placed in an ultrasound cleaner for 20 min to ensure complete dissolution. The PO$_4{}^{3-}$ supply phase (1 M) was prepared in a calibrated volumetric flask by the dilution of concentrated phosphoric acid.

3.3. LaPO$_4$:Ce^{3+}, Tb^{3+} Precursor Synthetic Process for the Membrane Reaction

The experiment was carried out in a glass cell system with self-adjusting diffusion which consisted of two glass units sandwiching a functional membrane ([C$_4$mim][BF$_4$] or [C$_4$mim][Tf$_2$N]). The glass units were filled with 50 mL of the rare earth mixture (rare earth sulfates or rare earth nitrates) at a certain ratio and 50 mL of the phosphoric acid solution (1 M). To ensure a homogeneous system, both solutions were stirred with a magnetic stirrer at 1000 rpm (Mini MR, IKA). After the complete reaction had occurred at room temperature, the white product was collected, centrifuged, and washed with ethanol more than 5 times, and then dried at 60 °C in a drying oven for 12 h to obtain the precursor. Under a set temperature (1000 °C), the LaPO$_4$:Ce, Tb precursor powder was calcined for 1 h under a reducing atmosphere to finally produced the green-emitting phosphors.

3.4. Characterization Methods

The concentration of P in the ultrapure water phase and the rare earth ion concentration of the LaPO$_4$:Ce^{3+}, Tb^{3+} samples were measured using a HORIBA-Jobin Yvon ULTIMA 2 series by inductively coupled plasma-atomic emission spectroscopy (ICP-AES). The Raman spectra were measured using the Horiba Jobin Yvon S.A.S. LabRAM Aramis. The structures and phase purities of the as-prepared LaPO$_4$:Ce^{3+}, Tb^{3+} samples were identified using X-ray diffraction analysis with a Bruker AXS D8 Advance Powder X-ray diffractometer (Cu Kα radiation, λ = 1.5418 Å). The morphologies, energy spectrum of membranes, and the as-prepared products were observed under a ZEISS SIGMA 500 field emission scanning electron microscope. The excitation and emission spectra were taken on an Edinburgh FLS980 spectrometer equipped with a 450 W ozone-free xenon arc lamp as the excitation source.

4. Conclusions

In summary, LaPO$_4$:Ce, Tb phosphors with monoclinic structures and good photoluminescence were successfully synthesized using a novel, controllable, and efficient ionic-liquid-driven supported liquid membrane system. The release rate of PO$_4^{3-}$ from the liquid membrane with different ionic liquids was different. The phosphors prepared by this method exhibited micro-spherical (when using rare earth sulfates as the raw material) and nanoscale stone-shape (when using rare earth nitrates as the raw material) morphologies due to the influence of the different anions. These studies indicate that ionic-liquid-driven supported liquid membrane systems are a promising method for preparing LaPO$_4$:Ce^{3+}, Tb^{3+} phosphors.

References

1. Eliseeva, S.V.; Bunzli, J.C. Lanthanide luminescence for functional materials and bio-sciences. *Chem. Soc. Rev.* **2010**, *39*, 189–227. [CrossRef] [PubMed]

2. Wang, G.; Peng, Q.; Li, Y. Lanthanide-Doped Nanocrystals: Synthesis, Optical-Magnetic Properties, and Applications. Accounts. *Chem. Res.* **2011**, *44*, 322–332. [CrossRef] [PubMed]

3. Richardson, F.S. Terbium(III) and Europium(III) Ions as luminescent probes and stains for biomolecular systems. *Chem. Rev.* **1982**, *82*, 541–552. [CrossRef]

4. Wang, N.; Zhang, S.; Zhang, X.; Wei, Y. Preparation of LaPO$_4$: Ce^{3+}, Tb^{3+} nanophosphors by mixed co-precipitation process and their photoluminescence properties. *Ceram. Int.* **2014**, *40*, 16253–16258. [CrossRef]

5. Niu, N.; Yang, P.; Wang, Y.; Wang, W.; He, F.; Gai, S.; Wang, D. LaPO$_4$:Eu^{3+}, LaPO$_4$:Ce^{3+}, and LaPO$_4$:Ce^{3+}, Tb^{3+} nanocrystals: Oleic acid assisted solvothermal synthesis, characterization, and luminescent properties. *J. Alloys Compd.* **2011**, *509*, 3096–3102. [CrossRef]

6. Yang, P.; Quan, Z.; Li, C.; Hou, Z.; Wang, W.; Lin, J. Solvothermal synthesis and luminescent properties of monodisperse LaPO$_4$:Ln (Ln=Eu^{3+}, Ce^{3+}, Tb^{3+}) particles. *J. Solid State Chem.* **2009**, *182*, 1045–1054. [CrossRef]

7. Hu, X.; Yan, S.; Ma, L.; Wan, G.; Hu, J. Preparation of LaPO$_4$: Ce, Tb phosphor with different morphologies and their fluorescence properties. *Powder Technol.* **2009**, *192*, 27–32. [CrossRef]

8. Yu, L.; Song, H.; Liu, Z.; Yang, L.; Lu, S.; Zheng, Z. Remarkable improvement of brightness for the green emissions in Ce^{3+} and Tb^{3+} co-activated LaPO$_4$ nanowires. *Solid State Commun.* **2005**, *134*, 753–757. [CrossRef]

9. Rao, R.P.; Devine, D.J. RE-Activated Lanthanide Phosphate Phosphors for PDP Applications. *J. Lumin.* **2000**, *87*, 1260–1263. [CrossRef]

10. Yu, M.; Lin, J.; Fu, J.; Han, Y.C. Sol–gel fabrication, patterning and photoluminescent properties of LaPO$_4$:Ce^{3+}, Tb^{3+} nanocrystalline thin films. *Chem. Phys. Lett.* **2003**, *371*, 178–183. [CrossRef]

11. Wang, Z.; Quan, Z.; Lin, J.; Fang, J. Polyol-Mediated Synthesis and Photoluminescent Properties of Ce^{3+} and/or Tb^{3+} Doped LaPO$_4$ Nanoparticles. *J. Nanosci. Nanotechnol.* **2005**, *5*, 1532–1536. [CrossRef] [PubMed]

12. Yu, M.; Wang, H.; Lin, C.K.; Li, G.Z.; Lin, J. Sol–gel synthesis and photoluminescence properties of spherical SiO$_2$@LaPO$_4$:Ce^{3+}/Tb^{3+}particles with a core-shell structure. *Nanotechnology* **2006**, *17*, 3245–3252. [CrossRef]

13. Dong, H.; Liu, Y.; Yang, P.; Wang, W.; Lin, J. Controlled synthesis and characterization of LaPO$_4$, LaPO$_4$:Ce^{3+} and LaPO$_4$:Ce^{3+}, Tb^{3+} by EDTA assisted hydrothermal method. *Solid State Sci.* **2010**, *12*, 1652–1660. [CrossRef]

14. Lenggoro, I.W.; Xia, B.; Mizushima, H.; Okuyama, K.; Kijima, N. Synthesis of LaPO$_4$:Ce, Tb phosphor particles by spray pyrolysis. *Mater. Lett.* **2001**, *50*, 92–96. [CrossRef]

15. Zhiqi, L.; Le, R.; Zhaowu, Z.; Dali, C.; Na, Z.; Minglai, L.; Meisheng, C.; Xiaowei, H. Synthesis of LaPO$_4$:Ce, Terbium by Co-Precipitation Method. *J. Rare Earths* **2006**, *24*, 137–140. [CrossRef]

16. Nunez, N.O.; Liviano, S.R.; Ocana, M. Citrate mediated synthesis of uniform monazite LnPO$_4$ (Ln = La, Ce) and Ln:LaPO$_4$ (Ln = Eu, Ce, Ce + Tb) spheres and their photoluminescence. *J. Colloid Interface Sci.* **2010**, *349*, 484–491. [CrossRef] [PubMed]

17. Song, W.-S.; Choi, H.-N.; Kim, Y.-S.; Yang, H. Formation of green-emitting LaPO$_4$:Ce, Tb nanophosphor layer and its application to highly transparent plasma displays. *J. Mater. Chem.* **2010**, *20*, 6929–6934. [CrossRef]

18. Song, W.-S.; Kim, Y.-S.; Yang, H. Construction of Highly Transparent Plasma Display Devices Using Hydrothermally Synthesized Green-Emitting LaPO$_4$:Ce, Tb Nanophosphors. *J. Electrochem. Soc.* **2011**, *158*, J137–J142. [CrossRef]

19. Duault, F.; Junker, M.; Grosseau, P.; Guilhot, B.; Iacconi, P.; Moine, B. Effect of different fluxes on the morphology of the LaPO$_4$:Ce, Tb phosphor. *Powder Technol.* **2005**, *154*, 132–137. [CrossRef]

20. Zhu, H.; Zhu, E.; Yang, H.; Wang, L.; Jin, D.; Yao, K. High-Brightness LaPO$_4$:Ce^{3+}, Tb^{3+} Nanophosphors: Reductive Hydrothermal Synthesis and Photoluminescent Properties. *J. Am. Ceram. Soc.* **2008**, *91*, 1682–1685. [CrossRef]

21. Yang, M.; You, H.; Liu, K.; Zheng, Y.; Guo, N.; Zhang, H. Low-temperature coprecipitation synthesis and luminescent properties of LaPO$_4$:Ln^{3+} (Ln^{3+} = Ce^{3+}, Tb^{3+}) nanowires and LaPO$_4$: Ce^{3+}, Tb^{3+}/LaPO$_4$ core/shell nanowires. *Inorg. Chem.* **2010**, *49*, 4996–5002. [CrossRef] [PubMed]

22. Ansari, A.A.; Khan, M.A.M. Structural and spectroscopic studies of LaPO$_4$:Ce/Tb@LaPO$_4$@SiO$_2$ nanorods: Synthesis and role of surface coating. *Vib. Spectrosc.* **2018**, *94*, 43–48. [CrossRef]

23. Dong, W.-L.; Zhang, X.-Y.; Shi, H.; Mi, X.-Y.; Wang, N.-L.; Han, K.-X. Synthesis and photoluminescence properties of LaPO$_4$:Ce^{3+}, Tb^{3+} nanophosphors by microwave-assisted co-precipitation method at low temperature. *Funct. Mater. Lett.* **2015**. [CrossRef]

24. Zhu, H.; Ou, G.; Gao, L. Hydrothermal synthesis of LaPO$_4$:Ce^{3+}, Tb^{3+}@LaPO$_4$ core/shell nanostructures with enhanced thermal stability. *Mater. Chem. Phys.* **2010**, *121*, 414–418. [CrossRef]

25. Fu, Z.; Bu, W. High efficiency green-luminescent LaPO$_4$:Ce, Tb hierarchical nanostructures: Synthesis, characterization, and luminescence properties. *Solid State Sci.* **2008**, *10*, 1062–1067. [CrossRef]

26. Hou, Z.; Wang, L.; Lian, H.; Chai, R.; Zhang, C.; Cheng, Z.; Lin, J. Preparation and luminescence properties of Ce^{3+} and/or Tb^{3+} doped LaPO$_4$ nanofibers and microbelts by electrospinning. *J. Solid State Chem.* **2009**, *182*, 698–708. [CrossRef]

27. Li, Y.; Chai, Q.; Liao, S.; Chen, Z.; He, Y.; Xia, Y.; Wu, W.; Li, B. Non-isothermal kinetics study with isoconversional procedure and DAEM: Thermal decomposition of LaPO$_4$:Ce,Tb·0.5H$_2$O. *Mater. Chem. Phys.* **2013**, *142*, 453–458. [CrossRef]

28. Zhang, Y.; Chen, J. Preparation of REPO$_4$ (RE = La-Gd) nanorods from an ionic liquid extraction system and luminescent properties of CePO$_4$:Tb^{3+}. *Rare Met.* **2016**. [CrossRef]

29. Bühler, G.; Stay, M.; Feldmann, C. Ionic liquid-based approach to doped nanoscale oxides: LaPO$_4$:RE (RE = Ce, Tb, Eu) and In$_2$O$_3$:Sn (ITO). *Green Chem.* **2007**, *9*, 924–926. [CrossRef]

30. Muntzeck, M.; Wilhelm, R. Influence of Ionic Liquids on an Iron(III) Catalyzed Three-Component Coupling/Hydroarylation/Dehydrogenation Tandem Reaction. *Int. J. Mol. Sci.* **2016**, *17*, 860. [CrossRef]

31. Park, J.; Jung, Y.; Kusumah, P.; Lee, J.; Kwon, K.; Lee, C.K. Application of ionic liquids in hydrometallurgy. *Int. J. Mol. Sci.* **2014**, *15*, 15320–15343. [CrossRef] [PubMed]

32. Lacrămă, A.M.; Putz, M.V.; Ostafe, V. A Spectral-SAR Model for the Anionic-Cationic Interaction in Ionic Liquids: Application to Vibrio fischeri Ecotoxicity. *Int. J. Mol. Sci.* **2007**, *8*, 842–863. [CrossRef]

33. Ramakul, P.; Mooncluen, U.; Yanachawakul, Y.; Leepipatpiboon, N. Mass transport modeling and analysis on the mutual separation of lanthanum(III) and cerium(IV) through a hollow fiber supported liquid membrane. *J. Ind. Eng. Chem.* **2012**, *18*, 1606–1611. [CrossRef]

34. Zhao, P.; Yang, F.; Zhao, Z.; Liao, Q.; Zhang, Y.; Chen, P.; Guo, W.; Bai, R. A simple preparation method for rare-earth phosphate nano materials using an ionic liquid-driven supported liquid membrane system. *J. Ind. Eng. Chem.* **2017**, *54*, 369–376. [CrossRef]

35. Bogdanowicz, K.; Sistat, P.; José, A.R.; Giamberini, M. Liquid crystalline polymeric wires for selective proton transport, part 2: Ion transport in solid-state. *Polymer* **2016**, *92*, 50–57. [CrossRef]

36. Shi, Y.; Wang, Y.; Wang, D.; Liu, B.; Li, Y.; Wei, L. Synthesis of Hexagonal Prism (La, Ce, Tb)PO_4 Phosphors by Precipitation Method. *Cryst. Growth Des.* **2012**, *12*, 1785–1791. [CrossRef]

37. Bühler, G.; Feldmann, C. Transparent luminescent layers via ionic liquid-based approach to $LaPO_4$:RE (RE = Ce, Tb, Eu) dispersions. *Appl. Phys. A* **2007**, *87*, 631–636. [CrossRef]

38. Pankratov, V.; Popov, A.I.; Chernov, S.A.; Zharkouskaya, A.; Feldmann, C. Mechanism for energy transfer processes between Ce^{3+} and Tb^{3+} in $LaPO_4$:Ce, Tb nanocrystals by time-resolved luminescence spectroscopy. *Phys. Status Solidi B* **2010**, *247*, 2252–2257. [CrossRef]

39. Pankratov, V.; Popov, A.I.; Kotlov, A.; Feldmann, C. Luminescence of nano- and macrosized $LaPO_4$:Ce, Tb excited by synchrotron radiation. *Opt. Mater.* **2011**, *33*, 1102–1105. [CrossRef]

40. Pankratov, V.; Popov, A.I.; Shirmane, L.; Kotlov, A.; Feldmann, C. $LaPO_4$:Ce, Tb and YVO_4:Eu nanophosphors: Luminescence studies in the vacuum ultraviolet spectral range. *J. Appl. Phys.* **2011**, *110*, 053522. [CrossRef]